Sudarshan Atmavilas, et. al. International Journal of Engineering Research and Applications
www.ijera.com
ISSN: 2248-9622, Vol. 12, Issue 9, September 2022, pp. 173-183

RESEARCH ARTICLE OPEN ACCESS

Thrust Response to RPM in Drone Blades with and without Dimples

Sudarshan Atmavilas*, Vishnu Paranganat**, and Sundaram Thirukkurungudi***
**(Academy of Science, Academies of Loudoun, Leesburg, VA 20175)*
***(Academy of Science, Academies of Loudoun, Leesburg, VA 20175)*
****(Academy of Science, Academies of Loudoun, Leesburg, VA 20175)*

Abstract
The COVID-19 outbreak has made the improvement of drone efficiency essential to facilitate automated delivery. Previous research has largely focused on using dimples to improve the aerodynamic efficiency of elliptical airfoils. The results of research on adding dimples to turbine blades has been largely inconclusive. Due to the lack of research on the effect of dimples on drone propellers and the increasing importance of drones, the number and the size of the dimples on the propellers were varied to determine the thrust response of the propellers to RPM. Propellers with different linear distributions of dimples were tested in Ansys Fluent, a computational fluid dynamics simulation, for their thrusts at different RPMs. Inlet velocity, viscous model, gravity, and enclosure size were all kept constant. Dimple number and dimple size had no significant effect on the thrust response to RPM in the drone propellers. Future research hopes to further explore the effects of crosswinds on drone propellers for different surface geometry modifications. This leads to the prediction that vortices due to dimples are overwhelmed by the turbulence generated by the rotary motion of the blades, subject to verification by future research.

Keywords: *Aerodynamics, dimples, drones, thrust, vortices*

Date of Submission: 10-09-2022 Date of Acceptance: 25-09-2022

I. Introduction

Drones are at the cutting edge of several industries, such as firefighting, cinematography, and the military, due to their growing potential along with lack of human risk. In only a few years, everyone's lives will be impacted by drones, especially with the recent advent of transportation, disinfectant spraying, and public safety monitoring drones during the coronavirus outbreak [1]. This makes optimizing the movement of drones through the air a pressing issue as humanity moves further into a technologically dominated landscape [2].

1.1 Background

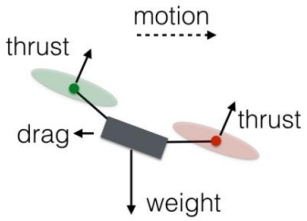

Figure 1: The thrust, drag, weight, and overall motion of a drone

A drone, or unmanned aerial vehicle (UAV), is an aircraft which does not carry a human pilot, but instead is either autonomous or remote-controlled from the ground [3]. A rotor or propeller is a rotating part of an aerial vehicle containing several airfoils that diverge outwards. Its rotation parallel to the ground generates the thrust that propels the craft upward into the air. The thrust of a rotor blade is dependent on both its geometry and external factors. The geometry of the blade can be designed and optimized, while external factors depend on the uncontrollable conditions of the airflow. Changing the geometry alters the way the rotor interacts with the surrounding fluid. Modifications in geometric design aim to reduce drag and increase thrust [4]. As seen in Figure 1, the net effect of the forward component of the thrust opposes the drag, while the net effect of the upward component of the thrust opposes the weight. When analyzing an individual rotor, the thrust directly opposes the drag.

Thrust is a systemic force that can be explained by Bernoulli's Principle in aerodynamic contexts. Essentially, it states that slower fluids tend to increase in pressure. When the airfoil moves

through a fluid, the shape of the airfoil distorts airflow in such a way that the airspeed below the airfoil is slower, causing a pressure gradient which leads to thrust [5].

When a smooth object moves through a fluid, it also possesses a boundary layer of fluid that follows the surface of the object, but this air detaches early from the surface and joins the fast-moving flow farther away from the object's surface, creating a detached flow or separated flow. This increases the area of the low-pressure zone behind the airfoil, known as the wake**,** which increases the pressure drag, as shown in Figure 2a. The positive effect of dimples, which are spherical impressions on a surface, on airflow can clearly be seen with modern golf balls, which is displayed in Figure 2b. As air flows past the surface dimples, tiny turbulence vortices are created on the golf ball's surface [6]. The turbulence pockets delay the boundary layer separation, and the surrounding airflow travels more tightly around the ball, creating a smaller wake [7].

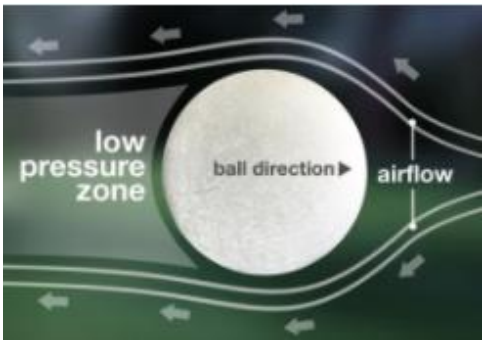

Figure 2a: Golf ball without dimples

Figure 2b: Golf ball with dimples

In the last decade, much research has been conducted on dimples on elliptical wing airfoils, with the consensus being that dimples reduce drag and increase aerodynamic efficiency [8]. Wind turbine blades are similar to drone blades, but are larger, differently shaped, and move in lower velocity air [9]. Some research has been geared towards wind and water turbines, but together the results have been inconclusive about the effect of dimples on efficiency.

A study researched the effect of dimple patterns on turbine blades. Researchers placed a row of dimples at different percentages of the length of the axial chord and found that dimples dramatically increased turbine efficiency and reduced the boundary layer separation [10]. This was furthered in a later study, in which researchers varied the size of dimples on a wind turbine airfoil and recorded the resulting lift and drag values. The smallest dimple size ended up producing the greatest lift-drag coefficient, begging the question as to whether dimples were even beneficial to turbine aerodynamics [11]. Then, another team researched the effects of dimples on wind turbine efficiency using computational software. When dimples were placed on the turbine blades, more power was generated, and efficiency increased [12]. Thus, the research community is still somewhat divided on this matter but is slowly coming to a consensus that dimples improve aerodynamic flow [13].

Figure 2b: Golf ball with dimples

Still, there have been other inconsistencies over the years. It was found that only the 5 rows of dimples nearest to the leading edge contributed to the formation of turbulent vortices, reducing drag, and dimples from the center of the surface increased drag [14]. This contradicted a study which suggested that, as dimples move toward the leading edge, maximum lift decreases and drag increases [15]. Researchers found that outward bumps were more efficient than inward dimples, with inward dimples actually producing more drag than a plain surface [16]. However, an inward dimple was found to produce a more efficient lift-drag ratio at a certain chord length than an outward bump [17]. Therefore, the relative effect of the number of dimple rows, the location of those rows on the airfoil, and the use of outward dimples as opposed to inward dimples require further investigation. Almost all of these previous dimple studies were performed on NACA (National Advisory Committee for Aeronautics) elliptical stationary airfoils, not propellers composed of rotating blades.

Usually drone blades have smooth surfaces to reduce friction and increase aerodynamic efficiency, but it is possible that adding surface features, such as dimples and bumps, could increase the thrust created by drone rotors if the "golf ball" effect prevails significantly. Other surface features, such as grooves, may also have similar positive aerodynamic effects [8]. Previously, measuring the thrust-to-power ratio by applying surface roughness to several surface areas of the blade showed that

increasing surface roughness resulted in less drag, greater lift, a higher thrust-drag ratio, and a greater stall angle [18]. This study did not investigate the competition between these dependent variables for surface roughness at different positions or degrees of roughness, and only studied helicopter blades that straighten due to an increase in rotation.

In software such as Autodesk Fusion 360, SolidWorks, or Onshape, surface alterations are easy to impose on an object due to the programs' ability to directly add or subtract shapes, such as spheres, from existing models. These programs produce models that can be used in software such as Ansys Fluent, which deals with computational fluid dynamics (CFD), the analysis of fluid mechanics and flows to solve real-world problems [19]. Ansys Fluent is found to be more reliable and accurate than the other most popular CFD software, STAR-CCM+, in yielding CFD results for both customized models and user chosen environment variables, though it can be slower [20].

II. EXPERIMENTAL DESIGN

The most effective arrangement will be the one in which dimples have the highest density per unit surface area in the blade, and are spaced very closely together, so that (i) the air moves closely along the surface, (ii) there is a turbulent flow, (iii) and the boundary layer separation is delayed as much as possible. The increase in dimples per unit surface area of the turbulent flow will increase the delay in the boundary layer separation, reduce the drag, and increase the lift, since the flow will remain very close to the body of the airfoil. Hence, the increase in the dimples per unit surface area of dimples will also increase the thrust and change the thrust-RPM response curve features. Therefore, it is reasonable to expect the greatest thrust to be produced by the arrangement with the greatest number of dimples and the largest size dimples.

H_0: The features of thrust-RPM response curves for different dimple numbers or dimple sizes all come from populations with equal medians.

H_A: The features of thrust-RPM response curves for different dimple numbers or dimple sizes do not all come from populations with equal medians.

A design of a press-fit bi-blade propeller was used as the base model and imported into Onshape, a cloud-based design modeling software [21]. The model was enlarged by a factor of 1.95 in Onshape so that its diameter would be 127.000 mm, and its center hole diameter would be 2.931 mm. Five different arrangements of dimples were created and placed on the base propeller design. Each arrangement varied the number of dimples in a single row, from 1 through 5. The numbers provided here to the third decimal in mm are obtained by converting the dimensions in Onshape from inches to metric units. The metric conversions were made to align all the measurements with the units of the data collected from Ansys Fluent.

Surface area density in this paper refers to the ratio of the amount of surface area covered by dimples to the total surface area of the propeller. For each arrangement, dimples were produced on the propeller using Onshape's Boolean subtraction feature. This feature was used to remove spheres from each of these points. Each sphere was inserted vertically onto the surface of the propeller until the center of the sphere rested on the surface, and then the sphere was subtracted from the surface. An example of a dimpled rotor propeller can be seen in Figure 3. Surface area density was changed using two different methods in the Onshape software. First, dimple size was kept constant while dimple number was varied incrementally, from 1 dimple to 5 dimples. Second, dimple number was kept constant as the radius of the dimple was varied incrementally from 0.195 mm to 0.780 mm. Accounting for both the change in the radius and number of dimples, the dimple surface area densities ranged from 0.0159% to 0.2544%.

The thickness of the propeller was approximately 1.140 mm, so the dimple radii were between 17.11% and 68.42% of the propeller thickness. The surface area of a single blade without dimples is 7.513 cm^2. A control model with no dimples was also created. In total, 15 models were created from varying the dimple number and size, disregarding the control. These 15 models were created through combinations of 4 different dimple sizes and 5 different numbers of dimples. Each model was then tested in Ansys Fluent to measure the thrust-RPM relationship within an enclosure.

The computational fluid dynamics environment was customized in the Ansys Fluent Workbench 2021 R1 software so that it could accommodate the propellers with different surface modifications using the dimples. A rectangular enclosure of width (x axis) 0.327 m, length (z axis) 1.015 m , and height(y axis) 0.327 m, was constructed in Ansys Fluent, which acts as a wind tunnel for the simulation. The enclosure itself is shown in Figure 5. The model propeller was placed into this wind tunnel and rotated. The axis of rotation was parallel to the z-axis. The resulting force vector acting on the propeller parallel to the z axis was recorded as the thrust force.

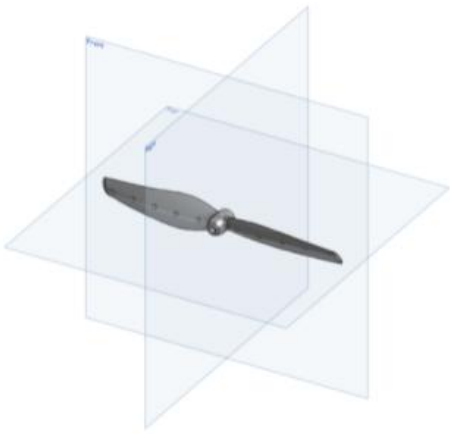

Figure 3: Propeller model with 5 dimples of radius 0.780 mm on each propeller

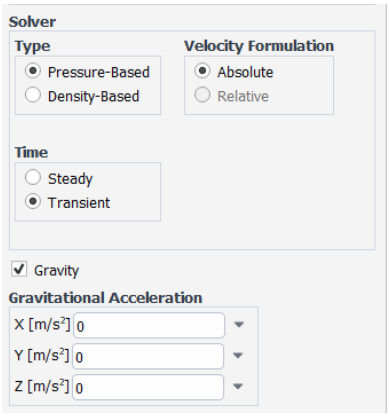

Figure 4: General parameter settings

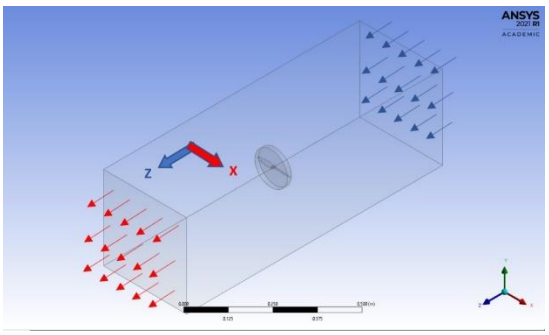

Figure 5: Force vector and axis directions, relative to the rectangular enclosure surrounding the simulated propeller

A pressure-based solver was used, since this is known to be more accurate when the flow is slow and incompressible, which means that its density doesn't change much in response to a change in its pressure. Since most of the domain would have a relatively low speed and not be rotating along with the propeller, the absolute velocity formulation setting was chosen. Since the properties and characteristics of the flow change with time, the flow time is transient. Gravitational acceleration was set to zero due to the numerous possible variations in the directions that propellers can face when they are used in drones. These settings are shown in Figure 4.

Turbulent kinetic energy (k) is the measure of how much kinetic energy is contained in the fluctuations. The fluctuations increase with increase in turbulent kinetic energy. Turbulent dissipation (ϵ) is the measure of the rate at which turbulent kinetic energy is dissipated. The k-epsilon (k-ϵ) model for turbulence is a two-equation model that attempts to simulate turbulent conditions [22]. It has two additional equations, one each for k and ϵ, which can be used to calculate the unknown turbulence terms. The k-epsilon model is particularly good at simulating small pressure gradients rather than large pressure gradients with complex flows. The k-epsilon model is part of the Reynolds-Averaged Navier Stokes (RANS) group of turbulence models [23].

There are several specific types of k-epsilon models, such as standard, RNG, and realizable [23, 24]. The realizable k-epsilon model is a variation of the k-epsilon model which changes two key parts of the equations. First, the transport equation for the dissipation rate is now based on the dynamic equation of the mean-square vorticity fluctuation. Second, a variable is changed in the eddy viscosity formula which helps avoid the violation of the Schwarz's inequality. The turbulent viscosity, Cμ, is assumed to be a variable, rather than a constant like in the standard k-epsilon model. These key changes allow the realizable k-epsilon model to better simulate and calculate the mean flow of large adverse pressure gradients and flows involving rotation [25].

The viscous model used to calculate the effects of turbulence in this paper is the realizable k-epsilon model with scalable wall functions, as shown in Equations 1 through 11. The realizable k-epsilon model measures turbulent kinetic energy, which is shown in Equation 1, and the rate of dissipation of the kinetic energy, as shown in Equation 2. The realizable k-epsilon differs most significantly from other k-epsilon models in Equation 2, by not containing the G_k term in the production term (pC_1S_e) to better model energy transfer and to prevent the destruction term (third term on the right-hand side) from becoming a singularity. This helps to improve the modelling for a larger range and different types of air flows.

To ensure that the wall function would be in the log-law region and that the cells would have a y+ value greater than 11.25, which is where the linear and nonlinear wall functions intersect,

scalable wall functions are used. This way, the cells in the simulation are scaled to make sure that the y+ value is large enough to use the log-law region, the region farthest from the wall that still moves slower than the free stream. The C2-Epsilon number is 1.9, the turbulent kinetic energy Prandtl number is 1, and the turbulent dissipation rate Prandtl number is 1.2, as displayed in Figure 6a. These values are used for the equation constants since they are the default values used by Ansys.

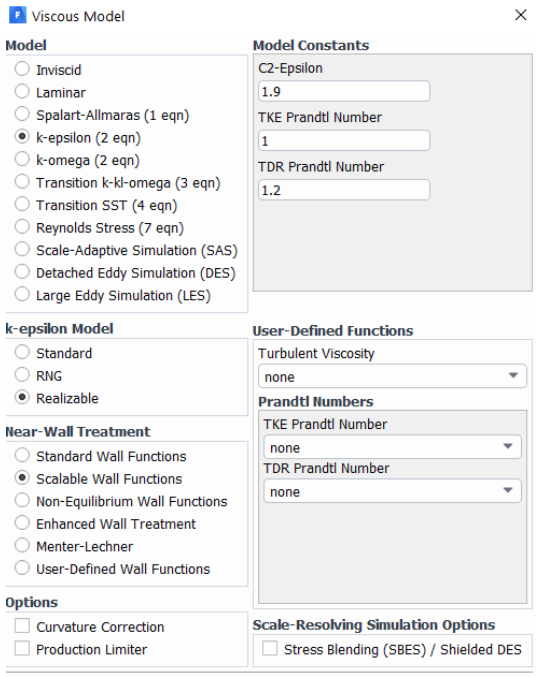

Figure 6a: Viscous model parameter settings

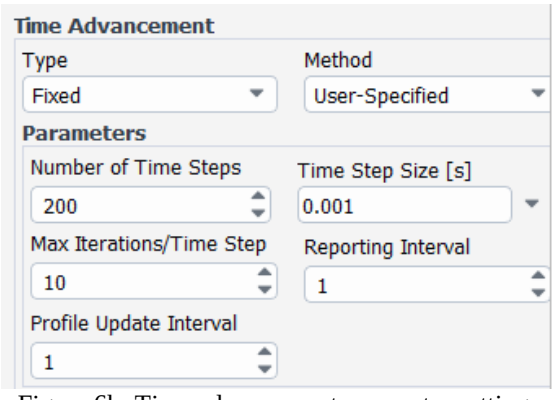

Figure 6b: Time advancement parameter settings

A Prandtl number represents the ratio between kinematic viscosity to thermal diffusivity. The TKE Prandtl number shows the ratio between the momentum diffusivity to the diffusivity of turbulence kinetic energy via turbulent transport, while the TDR Prandtl number shows the ratio between momentum diffusivity to the diffusivity of turbulent dissipation via turbulent transport. The Prandtl numbers are typically only used for thermal analysis, so the user defined Prandtl numbers in this case are none.

The following (1-11) are used to develop the model:

$$\frac{\partial}{\partial t}(\rho k)+\frac{\partial}{\partial x_j}(\rho k u_j)=\frac{\partial}{\partial x_j}\left[\left(\mu+\frac{\mu_t}{\sigma_k}\right)\frac{\partial k}{\partial x_j}\right]+G_k+G_b-\rho\epsilon-Y_M+S_k \quad (1)$$

$$\frac{\partial}{\partial t}(\rho \epsilon)+\frac{\partial}{\partial x_j}(\rho \epsilon u_j)=\frac{\partial}{\partial x_j}\left[\left(\mu+\frac{\mu_t}{\sigma_\epsilon}\right)\frac{\partial \epsilon}{\partial x_j}\right]+\rho C_1 S_\epsilon-\rho C_2\frac{\epsilon^2}{k+\sqrt{\nu\epsilon}}+C_{1\epsilon}\frac{\epsilon}{k}C_{3\epsilon}G_b+S_\epsilon \quad (2)$$

$$C_1=max\left[0.43,\frac{\eta}{\eta+5}\right],\qquad \eta=S\frac{k}{\epsilon},\qquad S=\sqrt{2S_{ij}S_{ij}} \quad (3)$$

$$\mu_t=\rho C_\mu\frac{k^2}{\epsilon} \quad (4)$$

$$C_\mu=\frac{1}{A_0+A_s\frac{kU^*}{\epsilon}} \quad (5)$$

$$U^*\equiv\sqrt{S_{ij}S_{ij}+\tilde{\Omega}_{ij}\tilde{\Omega}_{ij}} \quad (6)$$

$$\tilde{\Omega}_{ij}=\Omega_{ij}-2\epsilon_{ijk}\omega_k \quad (7)$$

$$\Omega_{ij}=\overline{\Omega_{ij}}-\epsilon_{ijk}\omega_k \quad (8)$$

$$A_0=4.04,\qquad A_s=\sqrt{6}\,cos\,\Phi \quad (9)$$

$$\Phi=\frac{1}{3}cos^{-1}(\sqrt{6}W),\qquad W=\frac{S_{ij}S_{jk}S_{ki}}{\tilde{S}^3},\qquad \tilde{S}=\sqrt{S_{ij}S_{ij}},\qquad S_{ij}=\frac{1}{2}\left(\frac{\partial u_j}{\partial x_i}+\frac{\partial u_i}{\partial x_j}\right) \quad (10)$$

$$C_{1\epsilon}=1.44,\qquad C_2=1.9,\qquad \sigma_k=1.0,\qquad \sigma_\epsilon=1.2 \quad (11)$$

In (1) and (2), G_k symbolizes the generation of turbulent kinetic energy due to the mean velocity gradients, while G_b symbolizes the generation of turbulent kinetic energy due to buoyancy. Y_M , seen in (1), represents how much the fluctuating dilatation in compressible turbulence contributes to the overall turbulent dissipation rate. C_2 and $C_{1\epsilon}$ in (2) and (3) are constants specific to the model. In (10), σ_k is the turbulent kinetic energy Prandtl number and σ_ϵ is the turbulent dissipation rate Prandtl number. S_k and S_ϵ are terms that can be custom defined by the user, as seen in (1) and (2). μ_t in (4) represents the eddy viscosity, and $\Omega_{ij}$from (6) and (7) represents the rotation rate tensor, as seen in a rotating reference frame with ω_k being the angular velocity. A_0 is a constant and A_s is a model constant, shown in (5) and (8). S_{ij} in (6) and (9) symbolizes the strain rate. Turbulent kinetic energy is represented by k and turbulent dissipation rate is represented by ϵ.

The under-relaxation factors are essential to the k-epsilon model of turbulence, as they control the stability of successive iterations. The following under relaxation factors were set: pressure as 0.3 Pa, density of air as 1 kg/m^3, body forces as 1 N, momentum as 0.7 kg·m/s, turbulent kinetic energy as 0.8 m^2/s^2, turbulent dissipation rate as 0.8 m^2/s^3, and turbulent viscosity as 1 Pa·s. The rotation-axis origin was set to the center of the x-y-z coordinate system, the rotation-axis direction was set to 1 for the z-axis, and the inlet velocity was set to zero, so that only the set RPM value would determine the motion of the propeller. The density of the propeller

was kept constant throughout the model at 1.115 g/cm$^{3.}$ Ansys Fluent simulated each model's rotation and measured each model's thrust response to the following RPMs: 3000, 4000, 5000, 6000, and 7000. To measure one thrust value for one RPM, the simulation ran in a fixed manner for 200 time steps at a time step size of 0.001 s, and with 10 iterations per time step. The reporting interval and the profile update interval were once every time step as shown in Figure 6b. A thrust-RPM trendline was generated for each propeller.

Two desktop computers were used to run the software needed to create the models and run the simulations. One PC had an Intel(R) Core (TM) i7-10700K 3.80 GHz processor, 32 GB of installed RAM, a 64-bit operating system, a x64-based processor, a Windows 10 Pro operating system, and an Intel UHD Graphics 630 GPU. The other PC had an AMD FX(tm)-6300 Six-Core 3.50 GHz processor, 32 GB of installed RAM, a 64-bit operating system, an x64-based processor, a Windows 10 Pro operating system, and a 2080 AMD GPU. Simulations were run on both the computers to verify whether there were any computational environmental differences in the results.

III. DATA

A test for one RPM value for a single propeller with a specific surface modification (dimple size and dimple number) consisted of 10 thrust values, each separated by two time steps. This process is then repeated for five different RPMs in order to complete the test for one propeller with a specific size and number of dimples. The propeller test is then repeated for each dimple number from 1 to 5 at a particular dimple size to complete a dimple number test. The dimple number test is then repeated for all dimple sizes (0.195 mm, 0.390 mm, and 0.780 mm), as well as for the control blade without dimples. In total, there are 10 thrust values per propeller-RPM combination, 50 thrust values for each propeller, 250 thrust values for each dimple size, 750 thrust values among all three dimple sizes, and 800 thrust values total including the 50 values part of the control blade without dimples. To save space, this paper provides in Table 1 only a sample of the data collectedfor one dimple number, one dimple radius, and one RPM. The researchers are willing to provide the complete data collected as needed.

Table 1: Sample data table showing the 10 thrust values for the propeller with 1 dimple on each blade, with a dimple radius of 0.195 mm and an RPM of 3000

Dimple Number	Dimple Radius (mm)	RPM	Trial Number	Thrust (N)
1	0.195	3000	1	0.1143683
1	0.195	3000	2	0.1136146
1	0.195	3000	3	0.1131524
1	0.195	3000	4	0.1132113
1	0.195	3000	5	0.1127369
1	0.195	3000	6	0.1144934
1	0.195	3000	7	0.1137579
1	0.195	3000	8	0.1132183
1	0.195	3000	9	0.1132548
1	0.195	3000	10	0.1127895
1	0.195	3000	Mean:	0.1134597
1	0.195	3000	Standard Deviation:	0.0005995

IV. RESULTS

First, the mean and standard deviation of each group of 10 thrust values were calculated. The five means for each combination of dimple number and radius were plotted on a thrust vs. RPM graph, as shown in Figures 7a, 7b, 7c, and 7d. The slopes and y-intercepts of each individual trendline were also found, as shown in Tables 2, 3, 4, and 5. These slopes and y-intercepts were used to compare the thrust-RPM relationships of different propellers, to see whether their thrust values responded differently to changes in RPM. Table 6 shows the compiled trendline results.

A Kruskal-Wallis nonparametric statistical test was chosen due to the unknown distribution of the data, and the likelihood that the median more accurately represents the center of the distribution than the mean. Each of the 10 thrust values for each dimple design, for each given RPM value, was considered to be a single sample in the Kruskal-Wallis test. For example, when the RPM was 3000, the 10 thrust values for the dimple radii of 0.195 mm, 0.390 mm, and 0.780 mm were used as the three different samples. Based on the calculation of the H-statistic and resulting p-value, it can be determined whether the samples likely come from populations with the same median. The Kruskal-Wallis nonparametric statistical test formula isshown in (12):

$$\mathrm{H} = \frac{12}{n(n+1)} \sum \frac{R_i^2}{n_i} - 3(n+1) \tag{12}$$

Table 2: Compiled thrust and trendline data for the propellers without dimples

Dimple Number	Dimple Radius (mm)	RPM	Mean Thrust (N)	Standard Deviation Thrust (N)	Trendline Slope (N/RPM)	Trendline Y-Intercept (N)
0	0.0000	3000	0.1095206	0.0004923		
0	0.0000	4000	0.1964260	0.0015267		
0	0.0000	5000	0.3066481	0.0003092		
0	0.0000	6000	0.4396403	0.0017120		
0	0.0000	7000	0.6138644	0.0084877	0.0001252	-0.2927

Table 3: Compiled thrust and trendline data for the propellers with a dimple radius of 0.195 mm

Dimple Number	Dimple Radius (mm)	RPM	Mean Thrust (N)	Standard Deviation Thrust (N)	Trendline Slope (N/RPM)	Trendline Y-Intercept (N)
1	0.195	3000	0.1134597	0.0005995		
1	0.195	4000	0.2028675	0.0014223		
1	0.195	5000	0.3174991	0.0008068		
1	0.195	6000	0.4561130	0.0013846		
1	0.195	7000	0.6164896	0.0022999	0.0001259	-0.2884
2	0.195	3000	0.1154847	0.0005321		
2	0.195	4000	0.2074128	0.0014501		
2	0.195	5000	0.3249282	0.0007750		
2	0.195	6000	0.4605992	0.0029532		
2	0.195	7000	0.6242058	0.0042243	0.0001271	-0.2888
3	0.195	3000	0.1142708	0.0005676		
3	0.195	4000	0.2041203	0.0014776		
3	0.195	5000	0.3197191	0.0008974		
3	0.195	6000	0.4589775	0.0018108		
3	0.195	7000	0.6188114	0.0040279	0.0001264	-0.2888
4	0.195	3000	0.1172972	0.0005426		
4	0.195	4000	0.2095725	0.0015730		
4	0.195	5000	0.3278016	0.0004447		
4	0.195	6000	0.4707113	0.0014658		
4	0.195	7000	0.6357717	0.0023225	0.0001298	-0.2968
5	0.195	3000	0.1173099	0.0003931		
5	0.195	4000	0.2055977	0.0014551		
5	0.195	5000	0.3253514	0.0015716		
5	0.195	6000	0.4662581	0.0025021		
5	0.195	7000	0.6337476	0.0041515	0.0001294	-0.2971

Table 4: Compiled thrust and trendline data for the propellers with a dimple radius of 0.390 mm

Dimple Number	Dimple Radius (mm)	RPM	Mean Thrust (N)	Standard Deviation Thrust (N)	Trendline Slope (N/RPM)	Trendline Y-Intercept (N)
1	0.390	3000	0.1142219	0.0010997		
1	0.390	4000	0.2038504	0.0015450		
1	0.390	5000	0.3201998	0.0019650		
1	0.390	6000	0.4533894	0.0025256		
1	0.390	7000	0.6163108	0.0030201	0.0001254	-0.2853
2	0.390	3000	0.1160679	0.0010931		
2	0.390	4000	0.2075123	0.0015801		
2	0.390	5000	0.3216627	0.0007542		
2	0.390	6000	0.4617832	0.0013377		
2	0.390	7000	0.6281528	0.0044244	0.0001278	-0.2922
3	0.390	3000	0.1201772	0.0010939		
3	0.390	4000	0.2104423	0.0018746		
3	0.390	5000	0.3238103	0.0017744		
3	0.390	6000	0.4670040	0.0029310		
3	0.390	7000	0.6280757	0.0044699	0.0001272	-0.2863
4	0.390	3000	0.1164252	0.0011383		
4	0.390	4000	0.2089268	0.0018440		
4	0.390	5000	0.3250114	0.0010640		
4	0.390	6000	0.4699095	0.0037878		
4	0.390	7000	0.6304614	0.0040031	0.0001289	-0.2944
5	0.390	3000	0.1162219	0.0007118		
5	0.390	4000	0.2092455	0.0009309		
5	0.390	5000	0.3272929	0.0014081		
5	0.390	6000	0.4680425	0.0017029		
5	0.390	7000	0.6359522	0.0019499	0.0001298	-0.2978

Table 5: Compiled thrust and trendline data for the propellers with a dimple radius of 0.780 mm

Dimple Number	Dimple Radius (mm)	RPM	Mean Thrust (N)	Standard Deviation Thrust (N)	Trendline Slope (N/RPM)	Trendline Y-Intercept (N)
1	0.780	3000	0.1143743	0.0004451		
1	0.780	4000	0.2055529	0.0015006		
1	0.780	5000	0.3167706	0.0012196		
1	0.780	6000	0.4520932	0.0026780		
1	0.780	7000	0.6159332	0.0025531	0.0001250	-0.2839
2	0.780	3000	0.1155440	0.0011121		
2	0.780	4000	0.2044371	0.0016655		
2	0.780	5000	0.3204451	0.0021483		
2	0.780	6000	0.4636039	0.0020900		
2	0.780	7000	0.6206989	0.0037704	0.0001269	-0.2898
3	0.780	3000	0.1151316	0.0011339		
3	0.780	4000	0.2062439	0.0016116		
3	0.780	5000	0.3213032	0.0021836		
3	0.780	6000	0.4614651	0.0023683		
3	0.780	7000	0.6190223	0.0037037	0.0001263	-0.2869
4	0.780	3000	0.1162296	0.0011521		
4	0.780	4000	0.2084058	0.0009966		
4	0.780	5000	0.3262489	0.0021404		
4	0.780	6000	0.4616592	0.0024483		
4	0.780	7000	0.6225410	0.0038109	0.0001266	-0.2859
5	0.780	3000	0.1144955	0.0037237		
5	0.780	4000	0.2016794	0.0057310		
5	0.780	5000	0.3125516	0.0046821		
5	0.780	6000	0.4554977	0.0042838		
5	0.780	7000	0.6059401	0.0026130	0.0001237	-0.2803

Table 6: Compiled trendline data for each dimple number, for all dimple sizes

Dimple Number	Trendline Slope (N/RPM)	Trendline Y-Intercept (N)
0	0.0001252	-0.2927
1	0.0001254	-0.2858
2	0.0001273	-0.2903
3	0.0001266	-0.2873
4	0.0001284	-0.2924
5	0.0001276	-0.2917

Table 7: Kruskal-Wallis Test Results

Kruskal-Wallis Test	H-Critical	H-Statistic	P-Value
Dimple Number	8.333	6.008	-
Dimple Size	5.991	4.415	0.11

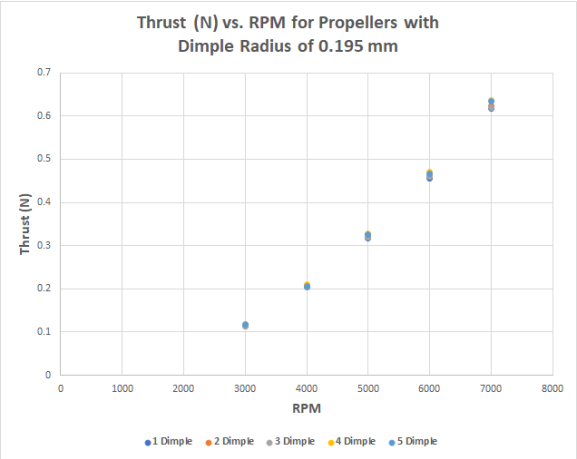

Fig. 7a: Thrust vs. RPM graph for 1-5 dimples with a dimple radius of 0.195 mm

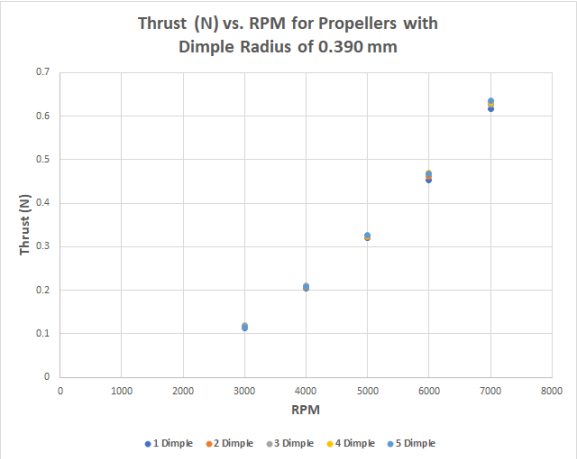

Fig. 7b: Thrust vs. RPM graph for 1-5 dimples with a dimple radius of 0.390 mm

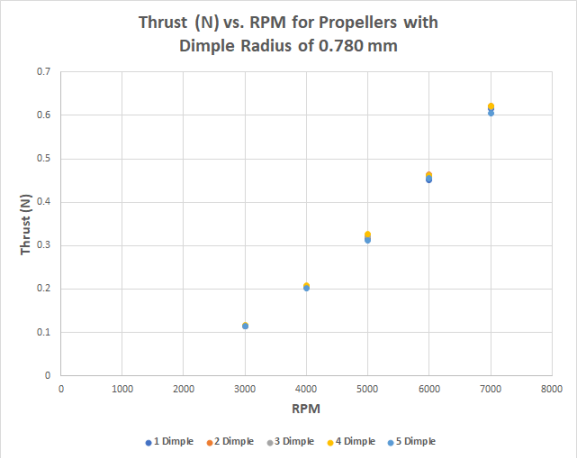

Fig. 7c: Thrust vs. RPM graph for 1-5 dimples with a dimple radius of 0.780 mm

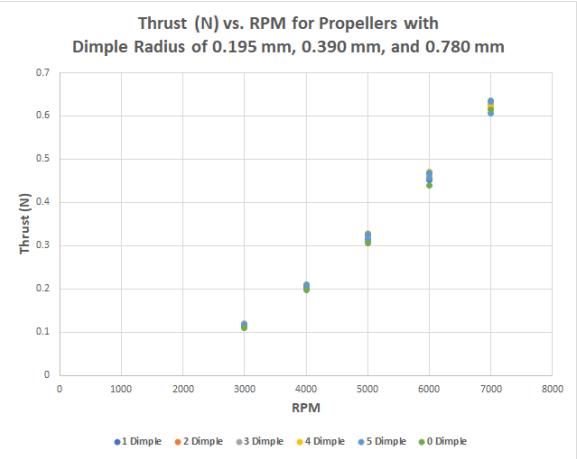

Fig. 7d: Thrust vs. RPM graph for 1-5 dimples with a dimple radius of 0.195 mm, 0.390 mm, and 0.780 mm

For (12), the Kruskal-Wallis formula for the H-statistic, the following symbols are representative of different quantities: n of the total number of samples, R_i of the sum of ranks from the i^{th} sample, H of the H-statistic, and n_i of the size of the i^{th} sample. In addition, when the sample sizes for all the samples was at least 5, the H-statistic was assessed using a Chi-distribution with the degrees of freedom set as 1 less than the number of samples. For sample sizes less than 5, the H-statistic must be compared with the H-critical to come up with a conclusion.

Due to the linear fit of the trendlines shown in Figures 7a, 7b, 7c, and 7d, the slopes of these trendlines were compared through statistical tests. While the slope directly represents the interaction between thrust and RPM, the x-intercept represents the threshold RPM value. This threshold value may represent more complex combinations of dissipative forces. In this simulation, the understanding of these complex forces is limited. Therefore, performing statistical analysis using either the x or y intercepts doesn't provide much insight into the behavior of the propellers. Since the best fit for all the response curves are linear, the only feature left to be compared using statistical analysis is the slope. The null hypothesis was that the slopes of different dimple numbers or sizes come from populations with equal medians, while the alternate hypothesis was that they all don't come from populations with equal medians. The first statistical test contains slopes from different dimple numbers of the same dimple size, while the second statistical test contains slopes from different dimple sizes of the same dimple number. The results of the statistical tests are shown in Table 7.

The first Kruskal-Wallis test assumes that the dimple size doesn't affect the thrust, and tests whether dimple number affects thrust. It contains 5 samples, with 1 sample for each dimple number. There were only 3 data points within each group, so there were not enough data points in each sample to assume a normal distribution, or consequently, to obtain a p-value. The degrees of freedom was 4, so the H-critical was 8.333. The H-statistic was 6.008, and since the H-statistic was less than the H-critical and outside of the rejection region, the null hypothesis was not rejected. The samples of different dimple numbers seem to come from populations with equal medians, and a change in dimple number doesn't seem to cause a significant change in the slope of the thrust-RPM trendline.

The second Kruskal-Wallis test assumes that the dimple number doesn't affect the thrust, and tests whether dimple size affects thrust. It contains 3 groups, with 1 sample for each dimple size and each group containing the five trendline slopes for five blades of one dimple size. The degrees of freedom was 2, so the H-critical was 5.991. The H-statistic was 4.415, producing a final p-value of 0.11. This is greater than the statistical significance value of 0.05, so the null hypothesis was not rejected.

Both Kruskal-Wallis tests failed to reject the null hypothesis. All slopes appear to come from populations with the same median. Since there is no significant change in the slope values due to changes in either dimple size or dimple numbers, one can confidently state that neither a change in dimple sizes nor dimple numbers will affect the thrust response to RPM. This can also be seen graphically in Figure 7d.

V. DISCUSSION

There was not a significant difference between the slopes of the thrust-RPM trendlines for different dimple numbers and dimple sizes. Table 6 shows that, while the dimple numbers of 0 and 1 produced smaller slope values, the dimple numbers of 2, 3, 4, and 5 produced slopes that do not show an observable trend. The y-intercepts of the trendlines shown in Tables 2, 3, 4, 5, and 6 were all similar, but were not compared using a statistical test since the physics of the y-intercept values is not clear beyond their source being in dissipative forces. An increase in RPM generally resulted in an increase in both the mean thrust and the standard deviation of the thrust as shown in Tables 2, 3, 4, and 5. The range of mean thrust values of the different propellers grew significantly as the RPM grew, as shown in Figures 7a, 7b, 7c, and 7d. As the RPM increased for any given dimple size, the range of mean thrust values across all of the dimple numbers significantly increased as well. These observations suggest that there is greater unpredictability associated with the turbulence generated by the motion of the propellers at greater RPM values, though they generally produce greater thrust.

Multiple thrust values for a single specific propeller-RPM combination were taken in order to properly sample the specific propeller-RPM thrust population. However, the inherent randomness of the simulation software due to the chosen turbulence model means that each simulation (and the 10 thrust values taken) is itself only a sample of a larger population of all simulations for that specific propeller and RPM. Though extensive sampling of the simulation population -- which requires an exorbitant amount of time -- is ideal, it is reasonable to assume that the variance within the simulation population was not significant due to the consistency of the results seen.

For a given RPM and number of dimples, as the dimple size increased, the range of the 10 thrust values calculated by the simulation also increased. While the mean of the 10 calculated thrust values was approximately the same across all the dimple sizes, larger dimples generally resulted in larger range of thrust values, and a larger standard deviation of thrust. This most likely indicates that larger dimples involve more complex aerodynamic principles that result in greater unpredictability in the results of the model. Since the focus of this study was not the cause and detailed nature of these ranges, it is deferred to future research.

The data points from Figures 7a, 7b, and 7c were combined to produce Figure 7d, which shows the same overall patterns in the thrust-RPM relationship. An increase in RPM raised the variation in thrust values produced, and an increase in RPM increased the thrust in a seemingly direct linear relationship. Similarly, Tables 2, 3, 4, and 5 were combined to produce Table 6, which displays that the slopes of the trendlines in Figure 7d are not significantly different, and do not show any observable patterns, even when compared to the trendline slope of the propeller without dimples.

A different set of statistical tests was also used on the data, on the individual data points themselves. 25 Kruskal-Wallis tests (1 for each of the 5 dimple numbers and each of the 5 RPMs) were run, each of which compared the 10 thrust values from each of the 3 dimple sizes. 19 out of the 25 tests rejected the null hypothesis and found that these thrust values come from populations with medians that are not all equal. While this might seem to be inconsistent with the current big-picture results shown in Table 7, these differences are simply smoothened out in the big picture by taking the mean thrust, calculating the slope of the mean thrusts, and comparing the slopes. These small-scale

differences are alleviated when the data is processed more heavily consistent with our original hypothesis. Future research may collect more data using multiple simulation runs to verify the extent to which these small-scale differences are significant enough to challenge the current conclusions using the means.

The lack of significant effect of the dimples on the thrust-RPM relationship may be explained by the overwhelming turbulence generated by the rotary motion of the blades in relation to the small vortices generated by the dimples. This turbulence generated by the rotating blades may have subdued the effects of the dimples so that they could not delay the boundary layer separation on the rotary blades. This is still subject to verification by future research, both through model calculations and experimental work of observing the airflow around the rotating blades with the dimples. Since all the results provided are based on a simulation hinged on a specific model, it is essential to obtain experimental verification of these results to add legitimacy to the results presented and to verify how close the values obtained from simulation are to the real values. In the event of there being a significant difference between future experimental results and the results in this research, further investigation may be warranted to verify whether it is caused by the experimental apparatus, the simulation, or the model itself.

VI. CONCLUSION

Based on the realizable k-epsilon model used in the Ansys Fluent simulation under the parameter settings shown in Figure 6a, which included scalable wall functions, C2-Epsilon = 1.9, TKE Prandtl Number = 1, TDR Prandtl Number = 1.2, and no turbulent viscosity, the results do not show any significant change in the thrust-RPM trendline for a linear distribution of dimples of different sizes and numbers. These simulation results are subject to verification by other simulation software and experiments.

The advantages of this research included its number of repeated trials and averaging of outputted values to produce the most representative data possible, and its variation in both number and size of dimples to identify the relative importance of both factors. Computational power was a major limitation of this paper. More powerful computers could have aided in more accurate simulations and significantly decreased the runtime. This would have allowed for a greater number of simulations, increasing the sample size, and therefore the confidence in capturing the population mean. The mean thrust values were calculated based on 10 thrust values provided from the same simulation after it reached stability. Future research could run the entire set of simulations repeatedly to verify whether the results are consistent with this research. The same model could also be simulated in other software to verify the results obtained in this research. These can determine whether the simulation results are consistent with the model used.

Though this research does not show any significant change in the thrust response curve due to dimples that are configured in a line on the blades, future research may attempt other configurations of dimple distributions and sizes to verify if dimples can have any effect at all on the thrust response curve. Adding different surface geometries can also be tested for further understanding of the aerodynamic mechanics behind the propeller-airflow interaction for application in future propellers.

ACKNOWLEDGEMENTS

The authors extend their gratitude to the Academies of Loudoun (ACL) for providing them with the facilities and resources to make this research possible.

REFERENCES

[1] How Drones Can Be Used to combat COVID-19. www.unicef.org/supply/media/5286/file/%20Rapid-guidance-how-can-drones-help-in-COVID-19-response.pdf.pdf, n.d.

[2] L. S. Dai, C. T. Pompei., M. A. Harary, S. L. Shan., and M. J. Tu, 3D printed quadcopters. NJ Governor's School of Engineering & Technology, 2016.

[3] K. Postigo. Multirotor Drone Control. ECE Senior Capstone. Department of Electrical and Computer Engineering, Senior Project Handbook, 2017. https://sites.tufts.edu/eeseniordesignhandbook/files/2017/05/Blue_Postigo_F1-1.pdf

[4] M. L. Sutkowy, and J. W. Gregory, *Relationship between rotor wake structures and performance characteristics over a range of low-reynolds number conditions, master's thesis*, Ohio State University. Columbus, OH, 2018.

[5] R. Qin. and C. Duan, The principle and applications of Bernoulli equation. *Journal of Physics: Conference Series, 916*, 2017, 012038.

[6] J. M. Mode, *Simulation of the flow over a flat dimpled plate*, master's thesis, Arizona State University, Tempe, AZ, 2010.

[7] J. M. Seeley, M. S. Crosser, J. Heath, and J. Murray, The drag coefficient of varying dimple patterns, senior thesis, Linfield College, McMinnville, OR, 2018.

[8] T. Golla, A. Muralikrishna, and S. Thirukkurungudi, Analyzing surface textures on elliptical wings. *International Journal of Engineering Research and Technology, 9(5)*, 2020.

[9] T. Letcher. Small scale wind turbines optimized for low wind speeds, Ohio State University, 2010.

[10] J. P. Casey, Effect of dimple pattern on the suppression of boundary layer separation on a low-pressure turbine blade, Air Force Institute Of Technology, Wright-Patterson Air Force Base, Ohio, 2004.

[11] S. K. Rasal and R. R. Katwate, International engineering research journal experimental and numerical investigation of lift and drag performance of NACA0012 wind turbine aerofoil. *International Engineering Research Journal, 4(6)*, 2017.

[12] K. K. Arun, V. R. Navaneeth, S. V. S. Kumar, and R. Ajay, Analyzing the effect of dimples on wind turbine efficiency using CFD. *International Journal of Applied Engineering Research, 13(6)*, 2018, 4484–4489.

[13] G. Fikade, A. Bekele, C. Venkatachalam, and M. Parthiban, Effects of dimples on aerodynamic performance of horizontal axis wind turbine blades. *International Research Journal of Engineering and Technology, 7(1)*, 2020, 525–539.

[14] C. Ramprasadh, and V. Devanandh, A CFD study on leading edge wing surface modification of a low aspect ratio flying wing to improve lift performance. *International Journal of Micro Air Vehicles, 7(3)*, 2015, 361–373.

[15] A. Ghoddoussi. A Conceptual Study of Airfoil Performance Enhancements using CFD. Wichita State University, Wichita, KS, 2011.

[16] D. Srivastav,. Flow control over airfoils using different shaped dimples. *International Proceedings of Computer Science and Information Technology, 33*, 2012, 92–97.

[17] P. A. A. Narayana, K. A. Rasya., and S. S. Prasad. Effect of outward and inward dimple located on different positions of aerofoil section at a typical low reynolds number. *International Journal of Engineering & Technology, 7(4)*, 2018, 29–34.

[18] W. N. W. Rohizan, A. S. M. Rafie, M. Y. Harmin, and C. C. Ciang, Effect of surface roughness on helicopter main rotor blade. *Innovation in Aerospace Engineering and Technology IOP Publishing, 152*, 2016, 12001.

[19] A. Jameson, L. Martinelli, and J. Vassberg, Using computational fluid dynamics for aerodynamics - A critical assessment. *23rd International Congress of Aeronautical Sciences*, Toronto, Canada, 2002.

[20] Y. Zou, X. Zhao, and Q. Chen, Comparison of STAR-CCM+ and ANSYS Fluent for simulating indoor airflows. *Building Simulation, 11(1)*, 2017, 165–174. https://doi.org/10.1007/s12273-017-0378-8

[21] E. Molina. (August 16th, 2019). 65mm press-fit bi-blade propeller with a 1.5mm center hole. https://grabcad.com/library/65mm-prop-1

[22] C. D. Scott-Pomerantz, *The K-Epsilon model in the theory of turbulence*, doctoral diss., University of Pittsburgh, Pittsburgh, PA, 2004.

[23] Z. J. Zhai, Z. Zhang, W. Zhang, and Q. Y. Chen, Evaluation of various turbulence models in predicting airflow and turbulence in enclosed environments by CFD: Part 1—Summary of prevalent turbulence models. *Hvac&R Research, 13(6)*, 2007, 853-870.

[24] T. M. Soe, and S. Y. Khaing, Comparison of turbulence models for computational fluid dynamics simulation of wind flow on cluster of buildings in mandalay, *International Journal of Scientific and Research Publications, 7(8)*, 2017, 337–350.

[25] J. Marcos, and D. Marshall, Improved computational and experimental validation using different turbulence models. *28th AIAA Applied Aerodynamics Conference*, San Luis Obs, CA, 2010.